LU-TP 23-052
May 2023

Glauber Monte-Carlo Simulation and Model Comparison in High-Energy Collisions

Sebastião Miranda

Department of Physics, Lund University

Bachelor thesis supervised by Christian Bierlich and Leif Gellersen

LUND
UNIVERSITY

Abstract

In this thesis, a Glauber Monte-Carlo event generator is developed and used to analyze proton-Ion (p -^{63}Cu and p -^{197}Au) and Ion-Ion (^{63}Cu -^{63}Cu and ^{197}Au -^{197}Au) collisions. Three different sub-collision models are implemented, the black disk, grey disk and oscillating grey disk models, and their validity is compared. The predicted nucleon-nucleon cross-sections by the different models are fitted to the experimental data and used as input for the Glauber simulation of the distribution of the number of participants in such collisions. This can be used to extract information about observables that show a high correlation with centrality.

Popular Science Summary

Even before science acquired its name, many minds were already concerned about what makes up the things that we see. In the search for these building blocks of nature, people had to come up with ways to have a closer look into the world. Magnifying glasses allowed us to see new details of our surroundings, optical microscopes enabled us to look into cells and big bacteria, moreover, the advent of particle accelerators allowed us to look at a completely new level of reality, bringing us closer to the indivisible.

By colliding particles at very high energies, particle accelerators allow us to study the extremely small particles that make up everything we see and the different forces that govern them. However, while looking through a magnifying glass is rather straightforward, and a trained eye is enough to make clear observations with a microscope, the results that come out of these collisions are much harder to analyse and validate or refute our theories.

Predicting the outcomes of these collisions is not a task that can be solved analytically most of the time. Instead, we can generate artificial collisions that work accordingly to theory and use these simulations to compare and interpret the experimental data extracted in large-scale accelerator experiments such as the Large Hadron Collider at CERN.

The aim of this thesis work is to create a simple event generator from scratch and use it to predict experimental observables according to different models that approximate theory in different levels of detail. These different models are then analyzed and compared in their capability of replicating already available data and their validity is discussed.

Contents

List of Figures

List of Tables

1 Introduction

Throughout the past decades, many breakthroughs have been made regarding our understanding of the constituents of matter. The increase in the energy scale of particle accelerators has allowed an increasingly detailed study of the building blocks of nature. However, this process has not only led to the answer to previous questions but also to the rise of many intriguing puzzles whose solutions are still waiting for the next generation of particle colliders to unveil.

There is a number of large-scale accelerator experiments projected to come into being during the next decades such as the Electron-Ion Collider, (EIC), at Brookhaven National Laboratory or the Future Circular Collider, (FCC), at CERN. The upgrade in the energy range of these accelerators will allow us to put the current theories to the test and have a closer than ever sight at nature.

In order to interpret and compare the experimental results from the accelerators with the current theoretical knowledge in particle physics it is necessary to have an expectation basis for the outcomes of such collisions that captures the theory in an accurate manner. In order to have such a basis, it is necessary to simulate particle collisions in a way that behaves in accordance with the theoretical frameworks being tested.

In this thesis work, a Glauber Monte Carlo approach is used to build a simple event-generator from scratch. The Glauber Model is a framework that simplifies the details of a collision to a small number of geometric quantities (e.g., how many nucleons participate in a proton-Ion collision, or how many nucleon-nucleon sub-collisions are there in an ion-ion collision) and is used to predict different observables (such as the scattering cross-sections) which can be compared with experiment [1]. To do such calculations analytically can be extremely complex, therefore, a Monte-Carlo approach, consisting of generating a large number of random events to infer the results from statistics is implemented. In addition, different models are implemented to generate sub-collisions, namely the black, grey and oscillating grey disk models. The calculated cross-section varies considerably among these models and their limitations in reproducing reality are discussed.

This report consists of a brief overview of the thesis work developed and is organized as follows. Firstly, the theoretical foundations are laid in section 2 introducing more details about the Glauber model, and the Good-Walker formalism used to calculate cross-sections and account for diffractive scattering. In section 3, the methodological approach is described introducing the practicalities of developing the simulation, such as how different nuclei are generated or how impact parameters are sampled. In subsection 3.3 different sub-collision models are introduced and the differences between these are explored in the rest of the report. Section 4 concerns the presentation and the discussion of the results regarding proton-proton, proton-ion and ion-ion collisions. Lastly, section 5 gives an overview of this thesis work and presents the next steps in enhancing our event-generator.

2 Theory

In this section a brief description of the theory behind the thesis work is given, starting with a general discussion on particle scattering and scattering cross-sections, followed by an introduction to the Glauber Model formalism, which is the main cornerstone of our simulation. This is followed by the presentation of the formalism necessary to calculate the scattering cross-sections in this model, the Good Walker formalism.

2.1 Particle scattering and cross-sections

There are different ways in which particles can collide and understanding the differences and the mechanisms that govern them is fundamental. Regarding kinetic energy conservation, there are two types of collision, elastic and inelastic. In elastic collisions, the kinetic energy of the system remains the same before and after the collision, whereas in inelastic collisions, part of the kinetic energy in the system is transformed. These transformations can result in the production of new particles or in the excitation of the particles into higher energetic states.

An inelastic collision can occur diffractively or non-diffractively. Diffractive scattering involves low momentum transfers and results in large rapidity gaps in the distributions of final state particles [2]. It is important to differentiate diffractive and non-diffractive inelastic collisions since the latter provides a larger contribution towards particle production.

One of the main concerns of this thesis is the calculation of the cross-sections of different processes. The cross-section, σ, is a measure of the likelihood for a collision to happen, more accurately, the *effective area of the target to interact with a projectile* [3]. Consider a beam with a large number of incident particles, N_{inc}, colliding with a target with density n_{tar}. The number of scattered particles, N_{sc}, is, on average:

$$N_{\text{sc}} = N_{\text{inc}}\ n_{\text{tar}}\ \sigma. \tag{1}$$

Similarly, we can consider the cross-sections for the different scattering processes described above:

$$\sigma_{\text{tot}} = \sigma_{\text{el}} + \sigma_{\text{inel}} = \sigma_{\text{el}} + \sigma_{\text{abs}} + \sigma_{\text{dif}}, \tag{2}$$

,

where, σ_{tot}, σ_{el}, σ_{inel}, σ_{abs} and σ_{dif} are, respectively, the total, elastic, inelastic, absorptive (inelastic non-diffractive) and diffractive cross-sections.

Cross-sections have units of area, typically given in barn, b. In SI units 1 b = 10^{-28} m^2. For the purpose of this thesis, the relevant cross-section magnitudes are on the order of mb (1 mb=0.1 fm^2).

2.2 Glauber Model

The Glauber model is a framework that can be used to calculate geometric quantities descriptive of a collision, such as the number of participating nucleons, N_{part}, and the number of binary sub-collisions, N_{coll} [1]. Although these quantities cannot be directly measured, they can be used to infer experimental observables such as the scattering cross-sections [1].

A few different inputs must be provided to perform such calculations. These are the nucleon-nucleon cross-section, $\sigma_{\text{inel}}^{NN}$, which can be measured *a priori*, and the nuclear charge densities. The latter will be discussed in section 3.1. An impact parameter, b, must be sampled from a realistic distribution and assigned to each collision. The details entailed in this process are discussed more thoroughly in section 3.2.

This model is built upon several assumptions. Firstly, the projectile's energy is high enough, such that its constituents carry enough momentum to be undeflected during their passage through the target. Secondly, the size of the target is large enough in comparison to the range of the nucleon-nucleon interaction. And thirdly, the target's constituents move independently. With these assumptions, a collision between a projectile and a target can be viewed in terms of the individual interactions between their parts. Another consideration is that, at the high energies considered, the projectile and target are lengths contracted in the beam direction such that they can be considered two-dimensional objects.

2.3 Good-Walker Formalism

The Good-Walker formalism allows for the calculation of the scattering cross sections for particles with well-defined wave functions and for the inclusion of diffractive scattering in these calculations. In the Good-Walker formalism, diffractive excitations result from fluctuations in the nucleon's partonic substructure [4].

Consider the nearly real amplitude operator, $\hat{T}$, related to the scattering S-matrix as $\hat{T} = 1 - \hat{S}$. In the high energy limit, the real part of the elastic amplitude, $\mathcal{A}_{\text{el}}$, vanishes and $T = -i\mathcal{A}_{\text{el}}$. Moreover, consider a complete set of normalized eigenstates $\{\psi_i\}$ of $\hat{T}(\vec{b})$ such that $\hat{T}(\vec{b})\,|\psi_i\rangle = T_i(\vec{b})\,|\psi_i\rangle$.

The wavefunction of the incoming beams, $|\psi_I\rangle$, can be expressed in terms of the projectile and target's wavefunctions $|\psi_p, \psi_t\rangle$:

[1] The number of binary subcollisions, N_{coll}, is the number of nucleon-nucleon subcollisions that occur as part of a collision process. Similarly, the number of participating nucleons, N_{part}, is defined as the sum of the nucleons in the target and the projectile that are involved in at least one sub collision. It is relevant to note that, in ion-ion collisions, N_{part} and N_{coll} might differ considerably, while in proton-ion and electron-ion collisions these two quantities only differ by one, $N_{\text{part}} = N_{\text{coll}} + 1$.

$$|\psi_I\rangle = \sum_{p=1}^{N_p} \sum_{t=1}^{N_t} c_p c_t \, |\psi_p, \psi_t\rangle \, . \tag{3}$$

The scattered wavefunction, $|\psi_S\rangle$, can then be inferred by applying the $\hat{T}$ operator on the incoming wavefunction:

$$|\psi_S\rangle = \hat{T}(\vec{b}) \, |\psi_I\rangle = \sum_{p=1}^{N_p} \sum_{t=1}^{N_t} c_p c_t T_{p,t}(\vec{b}) \, |\psi_p, \psi_t\rangle \, . \tag{4}$$

Hence, it is useful to define the profile function for elastic scattering, $\Gamma_{el}(\vec{b})$, in impact parameter space:

$$\begin{aligned} \Gamma_{\rm el}(\vec{b}) = \langle \psi_S | \psi_I \rangle = \sum_{p,t} |c_p|^2 |c_t|^2 T_{p,t}(\vec{b}) \, \langle \psi_p, \psi_t | \psi_p, \psi_t \rangle = \\ = \sum_{p,t} |c_p|^2 |c_t|^2 T_{p,t}(\vec{b}) \equiv \langle T_{p,t}(\vec{b}) \rangle_{p,t}, \end{aligned} \tag{5}$$

where the last step defines the average of the eigenvalues of $\hat{T}_{p,t}$ over all the target and projectile states.

Following these definitions, the elastic profile function can be related to the elastic collision cross-section:

$$\frac{{\rm d}\sigma_{el}}{{\rm d}^2\vec{b}} = |\Gamma_{\rm el}(\vec{b})|^2 = \langle T_{p,t}(\vec{b}) \rangle_{p,t}^2 \rightarrow \sigma_{\rm el} = \int {\rm d}^2\vec{b} \, \langle T_{p,t}(\vec{b}) \rangle_{p,t}^2. \tag{6}$$

The total and elastic cross-sections can be related by using the optical theorem. In reference [5], the optical theorem is formulated as:

$$\mathrm{Im}(\mathcal{A}_{\rm el}) = \frac{1}{2} \left\{ |\mathcal{A}_{\rm el}|^2 + \sum_j |\mathcal{A}_j|^2 \right\}, \tag{7}$$

where $\mathcal{A}_{el}$ is the elastic scattering amplitude and the sum runs over the scattering probabilities of the diffractive and non-diffractive inelastic channels. The expression inside the brackets is the total scattering probability.

Since in the high energy limit the real part of $\mathcal{A}_{el}$ vanishes, it follows from equation 7:

$$\frac{{\rm d}\sigma_{\rm tot}}{{\rm d}^2\vec{b}} = 2\Gamma_{el}(\vec{b}) = 2\langle T_{p,t}(\vec{b}) \rangle_{p,t} \rightarrow \sigma_{\rm tot} = 2 \int {\rm d}^2\vec{b} \, \langle T_{p,t}(\vec{b}) \rangle_{p,t}. \tag{8}$$

As can be seen above, given a $\langle T_{p,t}(\vec{b})\rangle_{p,t}$, it is possible to calculate the collision cross-sections. However, until now, the fluctuating states in projectile and nuclei have not been treated separately and the rest of this section aims at providing a way to do so.

Accounting for fluctuations

Since the wave functions of the target and the projectile are a superposition of eigenstates, the projectile can fluctuate, as well as the target. It is then essential to separate the fluctuations in the projectile and the target in order to obtain the right cross sections. In this subsection, the framework described before is expanded to account for such effects in accordance to reference [4].

The fluctuating projectile is assumed to be frozen in a state k during its passage through the target. We can then write the elastic scattering profile for the projectile in a fixed state k scattering on a target's nucleon as:

$$\Gamma_k(\vec{b}) = \langle \psi_S | \psi_I \rangle = |c_k|^2 \sum_t |c_t|^2 T_{t,k}(\vec{b}) \, \langle \psi_k, \psi_t | \psi_k, \psi_t \rangle = |c_k|^2 \sum_t |c_t|^2 T_{t,k}(\vec{b}) \equiv \langle T_{t,k}(\vec{b}) \rangle_t. \tag{9}$$

Averaging $\Gamma_k(\vec{b})$ over the possible projectile states during the collision recovers equation 8:

$$\sigma_{\text{tot}} = 2 \int \mathrm{d}^2 b \langle \langle T_{t,k} \rangle_p \rangle_t = 2 \int \mathrm{d}^2 b \langle T \rangle_{p,t}. \tag{10}$$

Since we are keen on collisions that contribute to particle production, it is more relevant to define a cross-section for a nucleon to be wounded in an interaction which does not account for elastic processes. Such a wounded cross-section is defined as in equation (7.7) of reference [4]:

$$\frac{\mathrm{d}\sigma_{\text{w}}}{\mathrm{d}^2 \vec{b}} = 2 \langle \langle T_{t,k} \rangle_p \rangle_t - \langle \langle T_{t,k} \rangle_t^2 \rangle_p \rightarrow \sigma_w = \int 2 \langle \langle T_{t,k} \rangle_p \rangle_t - \langle \langle T_{t,k} \rangle_t^2 \rangle_p \, \mathrm{d}^2 b. \tag{11}$$

If the models being implemented do not allow for a distinction between target and projectile excitations, the wounded cross-section is equivalent to the inelastic cross-section. However, if the model is accurate enough to allow for such a distinction, the wounded cross-section gives a more accurate picture of the likelihood of collisions resulting in particle production, since it accounts for the events where this results from diffractive excitation as well. Therefore, when the inelastic and wounded cross sections are not equivalent, the wounded cross section gives a more accurate input to the Glauber calculations.

3 Method

This section is concerned with giving a short summary of the implementation procedure of our Monte Carlo Glauber simulation. A deeper discussion about some of the topics mentioned before in this document is made, such as the method for generating nuclei, the method for sampling impact parameters, and the different collision models implemented.

3.1 Generating nuclei

The first step in creating this model is to generate the targets used in the Glauber simulation. The desired targets are large nuclei such as copper or gold and their charge density distribution $\rho(r)$ can be approximated by the Woods-Saxon distribution, which can be written as in reference [1] (without accounting for deviations from a spherical shape) :

$$\rho(r) = \frac{\rho_0}{1 + e^{\frac{r-R}{a}}}, \tag{12}$$

where ρ_0 is the nucleon density in the centre of the nucleus, r is the distance from the centre, R is the nuclear radius, and a is the nuclear thickness parameter.

For large nuclei with mass number A, the radius and thickness parameters in the equation above can be inferred, when the minimum distance between nucleons is $d = 0.9$ fm, using the parametrization in reference [6]:

$$R = 1.11A^{\frac{1}{3}} - 0.656A^{-\frac{1}{3}} \text{ [fm]}, \; a = 0.459 \text{ [fm]}. \tag{13}$$

In our implementation, the position of each nucleon is assigned as follows. First, the radial distance is randomly assigned from the distribution $\frac{\rho(r)}{\rho_0}r^2$ (more rigorously $4\pi\frac{\rho(r)}{\rho_0}r^2$ but the normalization can be dropped). Then, the azimuthal angle, ϕ is assigned by selecting a random number between 0 and 2π. Since the nucleons are uniformly distributed within a constant radius surface of the sphere, the polar angle, θ, is assigned as the arccosine of a random number between -1 and 1. Lastly, the condition for the minimum distance between two nucleons is checked and if there's no other nucleon at a distance smaller than d, the nucleon's position is assigned, otherwise, the process is repeated.

Figure 1 shows the normalized nucleon density $\rho(r)/\rho_0$ as a function of the distance to the centre of the nuclei, r, for ^{63}Cu and ^{197}Au. The histograms were created by combining 100000 copper nuclei and 10000 gold nuclei generated with the method described above. As can be seen for a sample size this big, the sampled nucleon density gives a close representation of the Woods-Saxon density distribution.

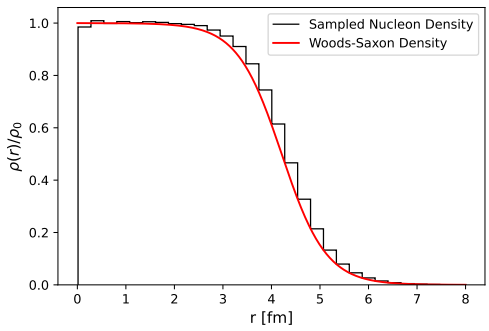

(a) ^{63}Cu nuclei.

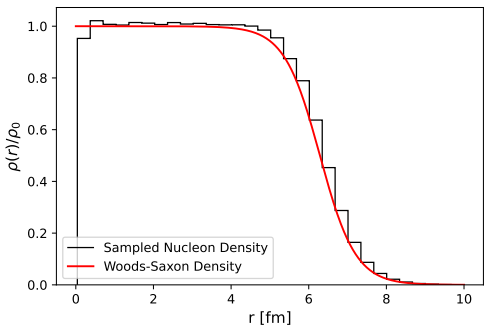

(b) ^{197}Au nuclei.

Figure 1: Monte Carlo generated nucleon density (in black) and Woods-Saxon density (in red), for ^{63}Cu and ^{197}Au nuclei.

3.2 Impact parameter sampler

Another fundamental element to be able to generate collisions is an impact parameter, b. Our event generator must be capable of randomly assigning an impact parameter to a collision from a realistic distribution. The probability of having an impact parameter close to 0 is much lower than having a large impact parameter on the periphery of the nucleus. This happens since there are no preferred angles in which the target can be hit, therefore, for a given impact parameter b any point of an infinitesimally wide annulus with radius b is equally likely to be hit. Consequently, the probability of assigning a certain impact parameter b is given by $f(b) = \mathrm{d}A/\mathrm{d}b = 2\pi b$. We want to sample from this distribution in an interval between 0 and a cutoff value b_{max}.

Consider a random number between 0 and 1, x_R, such that:

$$\int_0^b f(b)\ \mathrm{d}b = \mathrm{x}_R \int_0^{b_{max}} f(b)\ \mathrm{d}b. \tag{14}$$

If $y = F(b)$ is the primitive of $f(b)$ and F^{-1} is its inverse, then, we have:

$$b = F^{-1}\left(\mathrm{x}_R\ F(b_{max})\right) = \sqrt{\mathrm{x}_R\ b_{max}^2}\ . \tag{15}$$

In Figure 2 the outcome of the sampling method described above is shown for 10000 events.

3.3 Sub-collision models

Different models can be used to generate sub-collisions in Glauber Monte-Carlo simulations. These methodological contrasts produce major differences in the calculated cross-sections. In this thesis work, some of these are implemented and briefly presented in this subsection.

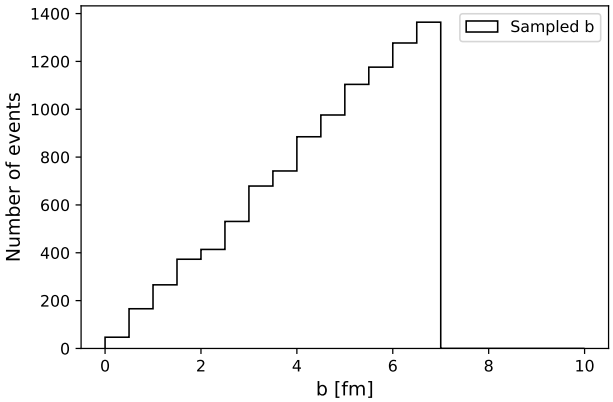

Figure 2: Histogram showing the sampled impact parameters for 10000 events with $b_{max} = 7$ fm.

3.3.1 Black disk model

In the black disk model, a radius, $r_{\text{bdisk}} = \sqrt{\sigma_{\text{inel}}^{\text{NN}}/\pi}$, is assigned to each of the target's nucleons. In the previous expression, $\sigma_{\text{inel}}^{\text{NN}}$ is the nucleon-nucleon inelastic cross section obtained *a priori*. If the projectile's distance to a target's nucleon is smaller than r_{bdisk} at any point of its passage, there is a collision between the projectile and that target's nucleon.

The black disk profile function for proton-proton collisions, $T^{pp}(b)$, is then 1 for $b \leq r_{\text{bdisk}}$ and 0 if $b \geq r_{\text{bdisk}}$, where b is now the impact parameter for a proton-proton collision. We can express this as in reference [5]:

$$T^{pp}(b) = \Theta(r_{\text{bdisk}} - b), \tag{16}$$

where Θ is the Heaviside step function.

By applying equations (6) and (8) on the black disk profile function expressed above, the expressions for the elastic and total cross-sections can be derived analytically:

$$\sigma_{\text{tot}} = 2\pi r_{\text{bdisk}}^2 = 2\sigma_{el}. \tag{17}$$

Despite not being the most realistic model, the implementation of the black disk model is a fundamental step in this work due to its simplicity. Moreover, this particular implementation allows for the validation of the method in an early stage of the implementation.

3.3.2 Grey disk model

The black disk model is a specific case of the more general grey disk model. In the latter, there is an extra parameter, α, that defines the opacity of the disk. The opacity parameter in this model directly scales the grey disk profile function, which can then be written as:

$$T^{pp}(b) = \alpha\Theta\left(r_{\text{bdisk}} - b\right). \tag{18}$$

Note that $0 \leq T^{pp} \leq 1$, therefore $0 \leq \alpha \leq 1$ such that unitarity is satisfied.

3.3.3 Oscillating grey disk model

Similarly to the grey disk described before there are two parameters defining this model, a radius, r_{bdisk}, and an opacity, α. However, in this model, when the projectile and target are within a radius r_{bdisk}, there is a probability α^2 that the two particles collide and the projectile is absorbed. This results in $\langle T_{p,t}^2(\vec{b})\rangle_{p,t} = \langle T_{p,t}(\vec{b})\rangle_{p,t}$ [5].

Due to the probabilistic nature of this collision model, the scattering amplitudes fluctuate. These fluctuations can be seen as the result of diffractive excitations in the projectile and target. Hence, this model allows us to calculate the diffractive scattering cross-section, σ_{dif}, for the first time.

The scattering cross-sections can be obtained as [5]:

$$\sigma_{\text{tot}} = 2\int \mathrm{d}^2\vec{b}\ \langle T_{p,t}(\vec{b})\rangle_{p,t} = 2\pi r_{\text{bdisk}}^2\alpha, \tag{19}$$

$$\sigma_{\text{el}} = \int \mathrm{d}^2\vec{b}\ \langle T_{p,t}(\vec{b})\rangle_{p,t}^2 = \pi r_{\text{bdisk}}^2\alpha^2, \tag{20}$$

$$\sigma_{\text{dif}} = \int \mathrm{d}^2\vec{b}\ \langle T_{p,t}^2(\vec{b})\rangle_{p,t} - \langle T_{p,t}(\vec{b})\rangle^2 = \pi r_{\text{bdisk}}^2\alpha(1-\alpha). \tag{21}$$

Equation 21 represents the total diffractive cross-section. This model allows us to differentiate between inelastic wounded nucleons and the nucleons that are wounded in non-diffractive inelastic processes, absorptively wounded nucleons. The absorptive cross-section is then:

$$\sigma_{\text{abs}} = \sigma_{\text{tot}} - \sigma_{\text{el}} - \sigma_{\text{dif}} = \pi r_{\text{bdisk}}^2\alpha = \frac{\sigma_{\text{tot}}}{2} \tag{22}$$

The choice of the cross-section to take as input for the Glauber calculations is not trivial and can vary depending on the observables being analyzed. The fact that this model does not allow for the separation of target and projectile excitations does not enable us to capture the full picture of the wounded nucleons resulting in particle production in proton-ion and ion-ion collisions. In a model separating the target and projectile's excitations, this could be achieved by using the definition of the wounded cross-section in equation 11.

This will be further discussed in section 4.2.

A representation of the profile functions for the three models mentioned above is seen in Figure 3.

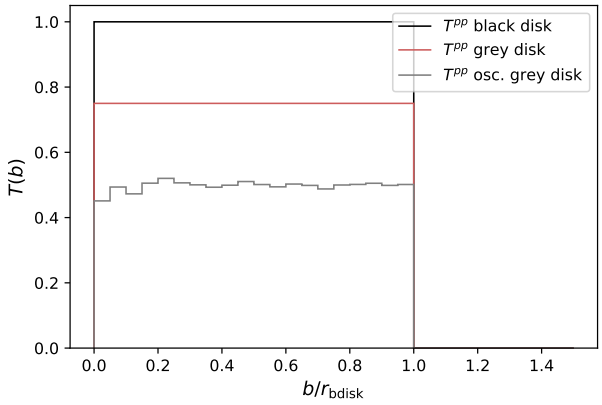

Figure 3: Profile function for black disk, grey disk ($\alpha = 0.75$) and oscillating grey disk ($\alpha = 0.5$).

3.3.4 On the energy dependence of the cross sections

In the models described above, the energy dependence is captured by two mechanisms. The first is the radial expansion of the projectile with energy which is reflected in the increase of r_{bdisk}. The second is the increase in matter density with energy, analogous to the increase in opacity, that eventually results in the saturation of the disk ($\alpha = 1$) leading to the black disk approximation [7].

The disk radius grows logarithmically and we parametrize it as:

$$r_{\mathrm{bdisk}}(s) = r_0 + \beta \log\left(\sqrt{\frac{s}{s_0}}\right), \tag{23}$$

where $s_0 = 1$ GeV, and r_0 and β are free parameters with units of length.

The disk radius parametrization in equation (24) is justified in reference [7] where a similar parametrization is used.

The opacity is considered to grow logarithmically:

$$\alpha(s) = \alpha_0 + \omega \log\left(\sqrt{\frac{s}{s_0}}\right), \tag{24}$$

with α_0 and ω as unitless free parameters.

The two previous functions are *ad-hoc* parametrizations found by us to be a good approximation of the experimental data and are important to perform the fitting of our models to the data in order to capture the energy dependence of the cross sections.

4 Results and Discussion

In this section, the results of our simulation for proton-proton, proton-ion and ion-ion collisions are presented and discussed.

The models described in the last section are implemented and their validity is compared.

4.1 Proton-Proton collisions

Initially, the free parameters in the models described in section 3.3 are fitted to the experimental data for the proton-proton total and elastic scattering cross-sections in reference [8]. The results of the fit are shown in Table 1 and a plot of the resulting cross-sections for the different models is shown in Figure 4.

	Black Disk	Grey Disk
r_0 [fm]	0.541 ± 0.003	1.29 ± 0.02
β [fm]	0.0778 ± 0.041	0.042 ± 0.002
α_0	-	0.17 ± 0.01
ω	-	0.041 ± 0.002

Table 1: Parameters obtained by fitting the black and oscillating grey disk models to the proton-proton cross-section data in [8].

The uncertainties in Table 1 correspond to the standard deviation of the fitted parameters.

The same fit is used for both grey disk models since the ratio $\sigma_{\text{tot}}/\sigma_{\text{el}}$ is the same in the two for the same opacity and radius.

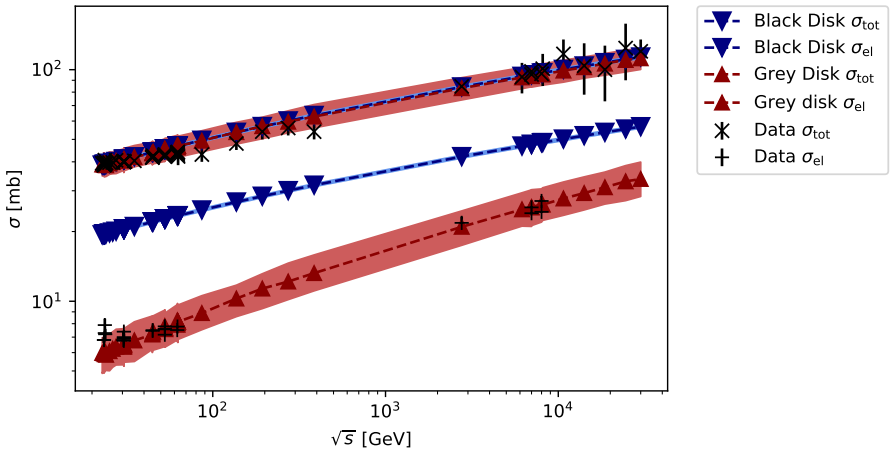

Figure 4: Plot of the energy dependence of the cross-section data in reference [8] and the fits of the black and oscillating grey disk models.

As can be seen in Figure 4, both the black and grey disk models give an accurate description of the total cross-section, however, the black disk model fails to describe the elastic cross-section. It should be noted that, for the results used in this section, the black disk model was fit to the σ_{tot} data. However, fitting the black disk model to the σ_{el} data would result in an accurate description of the elastic cross-section data instead. Since the ratio $\sigma_{\text{tot}}/\sigma_{\text{el}}$ is fixed and equal to 2 for the black disk model, the elastic and total cross sections cannot be accurately reproduced simultaneously. On the other hand, the grey disk model gives a good description of both the total and elastic cross-sections and their respective ratios.

From the parameterization described, we can calculate r_{bdisk} and α for the different collision models at any given energy. At a centre-of-mass-energy $\sqrt{s} = 200$ GeV, the radius of the black disk is $r_{\text{bdisk}} = 0.953 \pm 0.007$ fm, whereas for the grey disk models, a radius $r_{\text{bdisk}} = 1.51 \pm 0.04$ fm and an opacity $\alpha = 0.39 \pm 0.03$ is found. These results are used as input to calculate the proton-proton profile functions at $\sqrt{s} = 200$ GeV which are plotted as a function of impact parameter b in Figure 5.

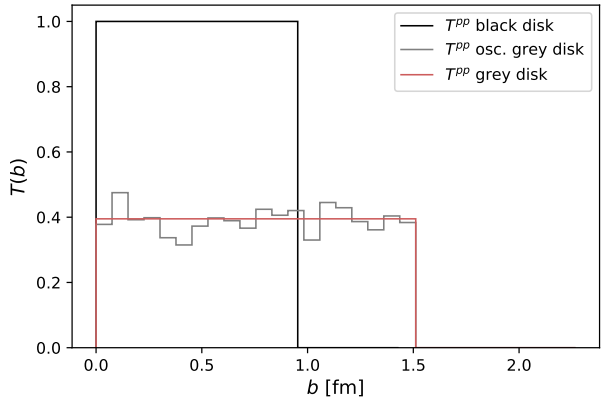

Figure 5: Profile functions for the black and oscillating grey disk model at $\sqrt{s} = 200$GeV as a function of impact parameter b. Monte-Carlo generated with 1000 events.

As can be seen in Figure 5, for the same energy, the black disk model shows a much narrower profile, while the grey disk model spreads into a larger radius. The elastic profile functions are used to calculate the different scattering cross-sections as described in the theory section. The results of this process can be seen in Table 2.

	Black disk	Grey disk	Osc. Grey disk
σ_{tot} [mb]	57.1 ± 1.9	56.7 ± 1.9	56.7 ± 1.9
σ_{el} [mb]	28.6 ± 0.9	11.2 ± 0.4	11.2 ± 0.4
σ_{inel} [mb]	28.6 ± 0.9	45.5 ± 1.5	45.5 ± 1.5
σ_{dif} [mb]	0	0	17.2 ± 0.6

Table 2: Cross-sections obtained for the different models at $\sqrt{s} = 200$GeV.

For fixed energies, the total cross-section is very close in the three models being discussed. On the other hand, the elastic cross-section is considerably higher for the black disk than for the grey disk models. Similarly, the inelastic cross-section is higher for the grey disk models, being about the same for the oscillating and non-oscillating models.

Despite these similarities in the two grey disk models, they present a fundamental difference since the diffractive cross-section is non-zero for the oscillating disk. As mentioned in section 3.3.3, for the latter model, it is possible to distinguish between inelastic and absorptive (inelastic non-diffractive) wounded nucleons.

However, since a correct treatment of the wounded nucleons that lead to particle production requires separating between the target and projectile's excitations as can be seen in equation (11), we are left with two options. Either we consider the diffractive contribution to the wounded cross-section to be negligible, and, by doing so we underestimate the wounded cross-section. Or, we consider the total inelastic cross-section as an input to the Glauber calculations which results in an over-estimation of the number of wounded nucleons resulting in particle production.

A quick look at equation (22) shows that $\sigma_{\text{tot}} = 2\sigma_{\text{abs}}$ for the oscillating grey disk model. Moreover, the black and grey disk models' fit to the total cross-section shows very similar results due to reasons discussed earlier in this section. Therefore, the absorptive cross-section in the oscillating grey disk model and the inelastic cross-section in the black disk model have very close values. This means that if the absorptive cross section would be used as input to the Glauber calculations, the results for the oscillating grey disk model would be equivalent to the ones predicted by the black disk model.

On the other hand, the use of the total inelastic cross-section as input for the Glauber calculations in the oscillating grey disk models results in the same predictions for the two grey disk models.

With this taken into account, the two grey disk models were chosen to be treated similarly when analyzing proton-ion and ion-ion collisions.

4.2 Proton-Ion collisions

Since the proton-proton and proton-neutron scattering cross-sections can be approximated to be the same resulting in $\sigma_{\text{inel}}^{NN} = \sigma_{\text{inel}}^{pp}$, we can now use the inelastic cross-sections calculated in the previous subsection as input to the Glauber calculations for proton-ion and ion-ion collisions.

Figure 6 shows the probability distribution for the number of wounded nucleons involved in proton-copper collisions for the black and grey disk models at different energies.

As can be seen in Figure 6, collisions with a smaller number of participants are much more likely than collisions with a higher number of participants. Collisions with the highest number of participants can be understood as being the most central since the copper's

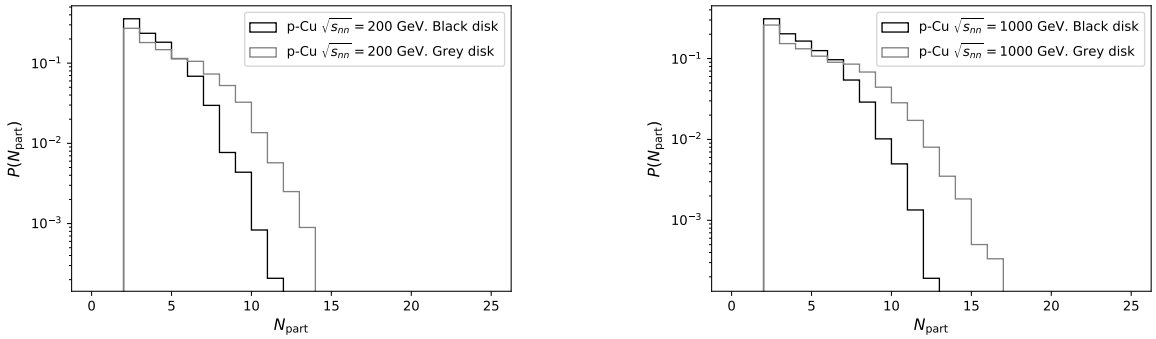

(a) $\sqrt{s_{nn}} = 200$ GeV. (b) $\sqrt{s_{nn}} = 1000$ GeV.

Figure 6: Probability distribution for the number of participants in proton-^{63}Cu collisions at $\sqrt{s_{nn}} = 200$ GeV and $\sqrt{s_{nn}} = 1000$ GeV and for the black and grey disk model.

charge density distribution follows a Woods-Saxon distribution and is highest closer to the centre of the nucleus as illustrated in Figure 3.1. The higher likelihood of having peripheral collisions can be understood as a consequence of the probability of assigning higher impact parameters being higher than assigning smaller impact parameters as illustrated in Figure 2. These two factors explain the shape of the distributions.

As can be noted in the observation above, there are close ties between the centrality and the number number of participants in a collision.

From Table 2 we can note that the grey disk model predicts a higher inelastic cross-section than the black disk model. This higher cross-section results in a larger disk radius since $r_{\text{bdisk}} = \sqrt{\sigma_{\text{inel}}/\pi}$, and, therefore, in a higher probability of getting a larger number of wounded nucleons in a collision. This explains why the grey disk model shows a higher probability for large values of N_{part} compared to the black disk model in Figure 6.

With an increase in the center-of-mass-energy of the collisions, there is an increase in the average number of participant nucleons due to the increase in the radii of both models and to the increase in opacity in the grey disk. At very high energies, as $\alpha \to 1$, the grey disk picture approximates the black disk.

It is important to note that, as mentioned in the previous subsection, the choice in the cross-section input affects the results considerably. As a consequence of this, the results displayed for the grey disk models reflect the choice that was done to approximate $\sigma_{\text{w}} \approx \sigma_{\text{inel}}$ in the oscillating grey disk model, resulting in the overestimation of the oscillating model's result in this section. A more accurate procedure is proposed in the conclusion section.

4.3 Ion-Ion collisions

This subsection shows the results of our Glauber simulation for Ion-Ion collisions in ^{63}Cu-^{63}Cu and ^{197}Au-^{197}Au collisions.

Figure 7 shows the average number of participants and sub-collisions as a function of the impact parameter in ^{63}Cu-^{63}Cu and ^{197}Au-^{197}Au collisions at different energies.

As can be seen, for fixed energies, the average number of participants is similar between the black and grey disk models, whereas the average number of collisions is considerably lower for the black disk. Due to the smaller radius of the black disk, each nucleon undergoes only a few collisions as is illustrated in Figure 7a where the ratio $N_{\text{coll}}/N_{\text{part}}$ is considerably smaller than in the grey disk counterpart displayed in Figure 7b. The same can be said by comparing Figure 7c with 7d, and Figure 7e with 7f. On the other hand, the number of participants does not significantly dependent on energy, yet it is considerably dependent on the centrality of the collision. As can be seen for the most central collisions it is fair to assume that at high energies, on average, every particle will interact at least once, since the projectile is close to fully overlapping with the target nuclei.

The growth in energy increases significantly the number of sub-collisions each participant undergoes due to the increase in the disk's radius. This can be seen by comparing Figure 7a with 7c and Figure 7b with 7d.

The increase in the atomic number of the colliding nuclei results in a higher number of participants and subcollisions as can be seen in Figures 7e and 7f showing gold-gold collisions, as expected.

Figure 8, shows the probability distribution for the number of participants simulated in ^{63}Cu -^{63}Cu and ^{197}Au -^{197}Au Collisions. Figures like these can be used to define centrality classes, and compared with the experimentally measured charge multiplicities.

As can be seen in Figures 8a and 8c the grey disk model shows a higher probability for higher participant numbers in the collisions than the black disk, again, due to the larger radius of the grey disk. As can be seen in Figures 8b and 8d, the grey disk starts approximating the black disk at higher energies as the opacity grows and the two radii get closer to each other in size.

Figure 8 shows the probability decreasing for a larger number of participants due to a higher probability of having peripheral events. A very high correlation between N_{part} and impact parameter exists as can be seen in Figure 7, and therefore, information about observables that show a high correlation with centrality can be extracted from these histograms.

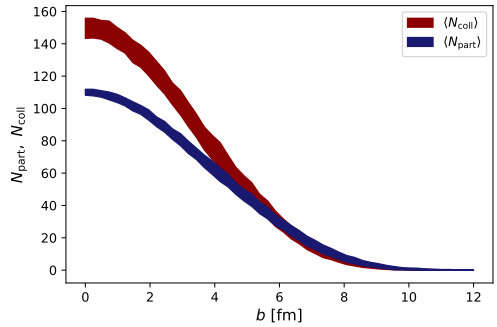

(a) ^{63}Cu-^{63}Cu $\sqrt{s_{nn}} = 100$ GeV Black disk

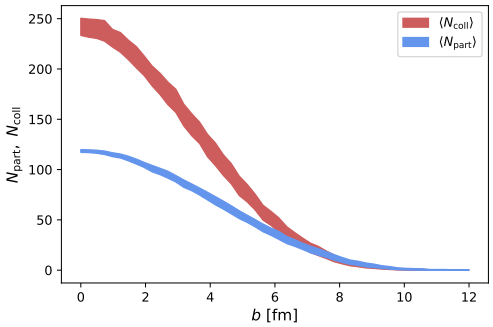

(b) ^{63}Cu-^{63}Cu $\sqrt{s_{nn}} = 100$ GeV Grey disk

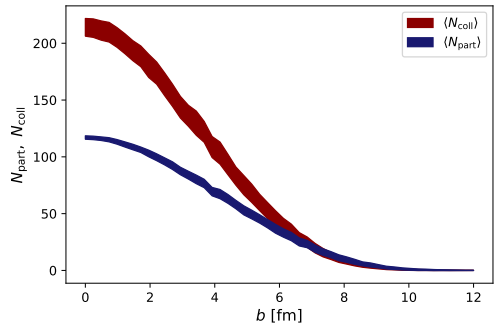

(c) ^{63}Cu-^{63}Cu $\sqrt{s_{nn}} = 1000$ GeV Black disk

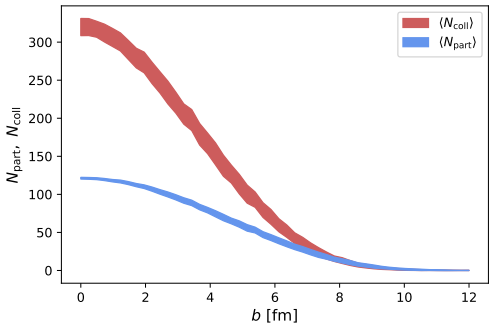

(d) ^{63}Cu-^{63}Cu $\sqrt{s_{nn}} = 1000$ GeV Grey disk

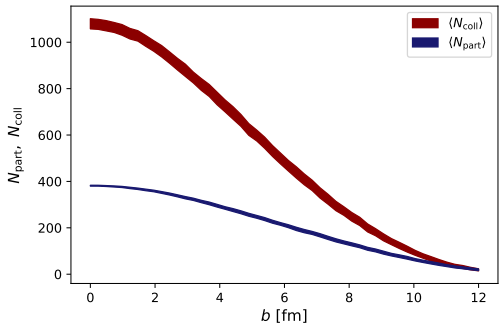

(e) ^{197}Au-^{197}Au$\sqrt{s_{nn}} = 1000$ GeV Black Disk

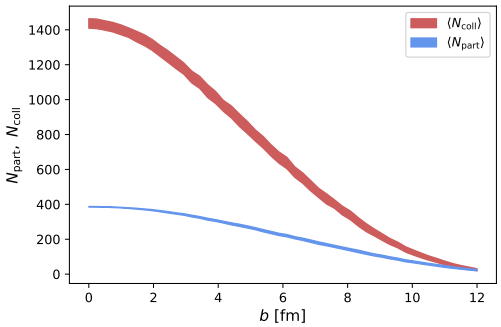

(f) ^{197}Au-^{197}Au $\sqrt{s_{nn}} = 1000$ GeV Grey disk

Figure 7: Average number of N_{part} and N_{col} dependence on impact parameter in ^{63}Cu-^{63}Cu and ^{197}Au-^{197}Au collisions for the black (on the left) and grey disk model (on the right) at different centre of mass energies.

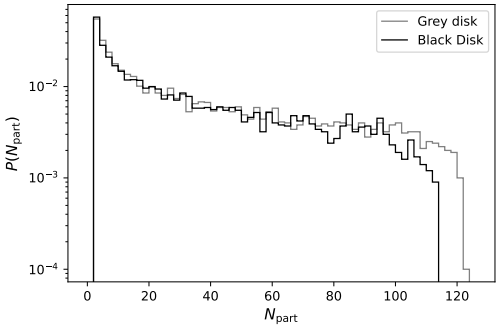

(a) ^{63}Cu-^{63}Cu $\sqrt{s_{nn}} = 100$ GeV

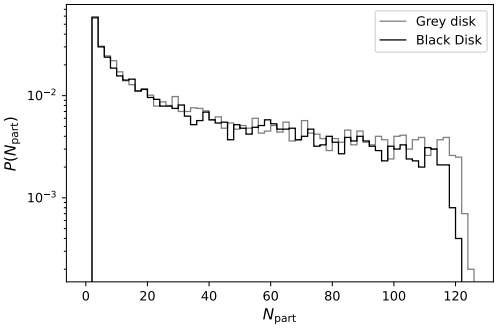

(b) ^{63}Cu-^{63}Cu $\sqrt{s_{nn}} = 1000$ GeV

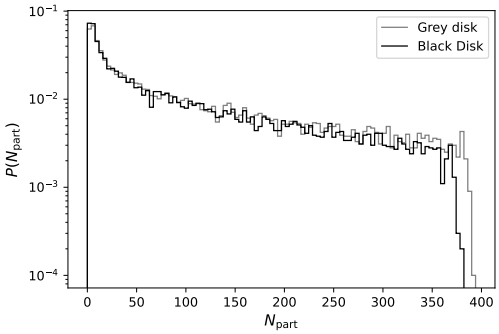

(c) ^{197}Au-^{197}Au $\sqrt{s_{nn}} = 100$ GeV

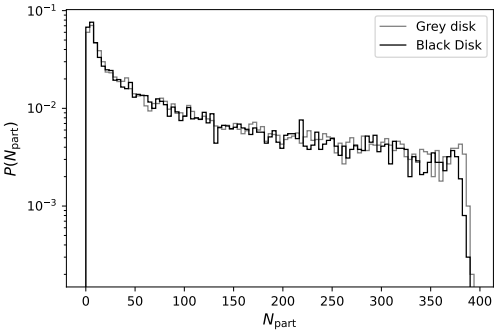

(d) ^{197}Au-^{197}Au $\sqrt{s_{nn}} = 1000$ GeV

Figure 8: Probability distribution for the number of participants in ^{63}Cu-^{63}Cu (on top) and ^{197}Au-^{197}Au (on the bottom) collisions at $\sqrt{s_{nn}} = 100$ GeV and $\sqrt{s_{nn}} = 1000$ GeV.

5 Conclusion and Outlook

Summarizing the work developed in this thesis, a Monte-Carlo Glauber simulation was developed and different sub-collision models were applied to the simulation of different types of collisions. Firstly, the energy dependence of the proton-proton cross-sections was fitted to experimental data for the black disk, grey disk and oscillating grey disk models. Then, the cross-sections for proton-proton scattering were used as input to calculate the probability distribution of the average number of participants in proton-Ion, and Ion-Ion collisions for the different models. The framework developed can be expanded to include more complex collision models and used to simulate γ^*-proton and electron-Ion collisions. A brief discussion on the next steps towards the development of our simulation is discussed in this section.

The choice of collision model critically affects the calculated cross-sections and the results of the Glauber calculations. The black disk model shows an underestimation of the inelastic cross-sections used as input for the Glauber calculations, outcoming a lower number of sub-collisions than the other models as can be seen in sections 4.1, 4.2 and 4.3. Moreover,

the grey disk model allows for a more accurate fit to the experimental data as can be seen in section 4.1, and, its oscillating version enables us to account for diffractive scattering, allowing us to distinguish between inelastic and absorptive wounded nucleons.

In the process of this thesis work, some first steps were done towards the inclusion of another model that could provide more accurate results and be applied in the simulation of electron-Ion collisions, This model consists in defining the target and projectile as a superposition of different grey disks (in the simplest case two disks) with different radii and opacities [5]. Each grey disk has a given weight reflecting the probability of it being assigned in a collision. This enables us to account for the different states that the projectile and target can be in. This separation of the excitations in projectile and target allows us to apply the formalism in subsection 2.3 to calculate the wounded cross-section in equation (11) and use it as an input of the Glauber calculations reflecting a more accurate picture of the wounded nucleons that result in particle production.

Due to time limitations, it was not possible to reach the desired level of development in this model and therefore it was left out of this report. Also, the formalism can be expanded to treat γ^*-proton and electron-ion collisions, however, only by having a model that separates the excitations in target and projectile, such as the one described above, it is possible to capture such collisions accurately.

In conclusion, the event generator developed shows satisfactory results that can be refined with the inclusion of more complex models and by accounting for deformations in the nuclei shape not considered in our work. The guidelines for future work presented can greatly enhance the results produced by our simulation and allow for the simulation of other types of collisions.

References

[1] Michael L. Miller et al. "Glauber modeling in high energy nuclear collisions". In: *Ann. Rev. Nucl. Part. Sci.* 57 (2007), pp. 205–243. DOI: 10.1146/annurev.nucl.57.090506.123020. arXiv: nucl-ex/0701025.

[2] Nicolò Cartiglia. "Measurement of the proton-proton total, elastic, inelastic and diffractive cross sections at 2, 7, 8 and 57 TeV". In: (May 2013). arXiv: 1305.6131 [hep-ex].

[3] J.R. Taylor. *Classical Mechanics*. University Science Books, 2005. ISBN: 9781891389221.

[4] Christian Bierlich and Christine O. Rasmussen. "Dipole evolution: perspectives for collectivity and γ^*A collisions". In: *JHEP* 10 (2019), p. 026. DOI: 10.1007/JHEP10(2019)026. arXiv: 1907.12871 [hep-ph].

[5] Christian Bierlich, Gösta Gustafson, and Leif Lönnblad. "Diffractive and non-diffractive wounded nucleons and final states in pA collisions". In: *JHEP* 10 (2016), p. 139. DOI: 10.1007/JHEP10(2016)139. arXiv: 1607.04434 [hep-ph].

[6] Maciej Rybczynski et al. "GLISSANDO 2 : GLauber Initial-State Simulation AND mOre..., ver. 2". In: *Comput. Phys. Commun.* 185 (2014), pp. 1759–1772. DOI: 10.1016/j.cpc.2014.02.016. arXiv: 1310.5475 [nucl-th].

[7] R. Conceicao, J. Dias de Deus, and M. Pimenta. "Proton-proton cross-sections: the interplay between density and radius". In: *Nucl. Phys. A* 888 (2012), pp. 58–66. DOI: 10.1016/j.nuclphysa.2012.02.019. arXiv: 1107.0912 [hep-ph].

[8] Particle Data Group et al. "Review of Particle Physics". In: *Progress of Theoretical and Experimental Physics* 2022.8 (Aug. 2022). 083C01. ISSN: 2050-3911. DOI: 10.1093/ptep/ptac097. eprint: https://academic.oup.com/ptep/article-pdf/2022/8/083C01/49175539/ptac097.pdf. URL: https://doi.org/10.1093/ptep/ptac097.